Effect of Fan on Inlet Distortion: A Mixed-fidelity Approach

Yunfei Ma*
Department of Engineering, University of Cambridge, United Kingdom, CB2 1PZ

Jiahuan Cui†
School of Aeronautics and Astronautics, and ZJU-UIUC institute, Zhejiang University, People's Republic of China, 310007

Nagabhushana Rao Vadlamani‡
Department of Engineering, University of Cambridge, United Kingdom, CB2 1PZ

Paul Tucker§
Department of Engineering, University of Cambridge, United Kingdom, CB2 1PZ

Inlet distortion is typically encountered during off-design conditions on civil aircraft and in S-ducts in military aircraft. It is known to cause severe deterioration to the performance of a gas-turbine engine. As intakes become shorter, there is an increased interaction between the inlet distortion and the downstream fan. Previous studies in the literature use RANS or URANS to model this unsteady interaction, due to the substantial computational cost associated with high-fidelity methods such as LES/DNS. On the other hand, it is well known that turbulence models have limitations in terms of predicting distorted flows. In this paper, we propose a mixed-fidelity approach and employ it to study the intake-fan interaction at an affordable computational cost. The results demonstrate that there are two mechanisms via which the fan affects the separated flow. Firstly, the suction effect of the fan (effective up to almost half of the chord length upstream of the fan) alleviates the undesired distortion by 'directly' changing the streamline curvature, intensifying the turbulence transport and closing the recirculation bubble at a much earlier point in time. Secondly, the enhanced turbulence in the vicinity of the fan feeds back into the initial growth of the shear layer by means of the recirculating flow. This 'indirect' feedback is found to increase turbulence production during the initial stages of formation of the shear layer. Both the direct and indirect effects of the fan significantly suppress the inlet distortion.

Nomenclature

*PhD candidate, Department of Engineering, ym324@cam.ac.uk
†Assistant Professor, School of Aeronautics and Astronautics, jiahuancui@intl.zju.edu.cn
‡Senior Research Associate, Department of Engineering, nrv24@cam.ac.uk
§Professor, Department of Engineering, pgt23@cam.ac.uk, Associate Editor

ρ	=	density
$\boldsymbol{u}$	=	velocity
p	=	pressure
x	=	x coordinate
$\boldsymbol{x}_0$	=	body/surface coordinate
$\boldsymbol{f}$	=	force
α,β	=	feedback force coefficients
$\boldsymbol{n}$	=	normal vector to the blade surface
t	=	time or blade thickness
K	=	viscosity coefficient of parallel force
k_1	=	coefficient for viscosity distribution
Δy_+	=	dimensionless wall distance
Δx_+	=	dimensionless streamwise distance
Δz_+	=	dimensionless spanwise distance
λ	=	blockage factor
E	=	Internal Energy
D	=	side of the triangular prism
H	=	height of the beam
H_e	=	Enthalpy
Q	=	Q-criterion
$\left\langle u_i' u_j' \right\rangle$	=	Reynolds stresses
a_{ij}	=	anisotropy tensor
δ_{ij}	=	Kronecker delta
i, j	=	index
C_{ic}	=	coefficients for Barycentric map
R	=	resolution in Komogorov units
V	=	cell volume
ε	=	TKE dissipation
$\mathcal{P}$	=	TKE production
C	=	TKE convection
CFD	=	Computational Fluid Dynamics
PDE	=	Partial Differential Equation

RANS = Reynolds Averaged Navier-Stokes

URANS = Unsteady Reynolds Averaged Navier-Stokes

LES = Large Eddy Simulation

DNS = Direct Numerical Simulation

BFM = Body Force Method

IBM = Immerse Boundary Method

IBMSG = Immersed Boundary Method with Smeared Geometry

SA = Spalart-Allmaras

RHS = Right Hand Side

TKE = Turbulent Kinetic Energy

RGB = Red, Green and Blue

I. Introduction

Flow distortion is typically encountered within the engine intakes and in the duct flows under off-design conditions. The flow over an intake lip can separate during the take-off of an aircraft at an extremely large angle of incidence and under severe crosswinds during taxiing or landing. The distorted flow at the inlet convects downstream and results in a deterioration of the performance of the fan. In some extreme cases, it can even lead to catastrophic events such as stall and surge. Interestingly, as inlets have become shorter, the presence of a fan has also been shown to affect the distortion recovery ([1]). In order to numerically investigate this interaction, it is crucial to accurately resolve the following flow phenomena: (a) the separated flow region and (b) the influence of a fan.

Most research in the literature has addressed the study of fan-distortion using URANS or RANS [2–4]. It is well known that the accuracy of these turbulence models are satisfactory at the design point. However, they still suffer from severe limitations under off-design conditions, including flow separation, distortion and unsteadiness [5–7]. In particular, when predicting large-scale vortical flows, the results may vary significantly when different RANS models are employed [5, 8]. For these flows, eddy resolving simulations such as DNS/LES and hybrid RANS–LES are demonstrated to yield much more promising results [9–11].

The influence of the fan can be represented either by resolving all fan blades or with a modelled force using the Immersed Boundary Method (IBM). IBM does not necessarily reduces the mesh size, but as an advantage, the meshing of complex blade geometries becomes obsolete. It renders the process of mesh generation significantly more efficient, enabling exploration of more complex geometries. Its derivative, the Immersed Boundary Method with Smeared Geometry (IBMSG), can be also applied based on the requirements of the flow and the computational cost.

The standard IBM is generally used to resolve the features of stationary or moving objects. This idea was first

proposed by Sirovich [12], who applied it to solve linearised initial and boundary problems. He regarded the boundary surface as a distribution of sources which could be directly included in the Navier–Stokes equations. Consequently, these problems can be converted to conventional PDEs with source terms. Peskin [13] then rigorously demonstrated this method based on Eulerian and Lagrangian variables, linked by the interaction equations involving the smooth approximation of the Dirac-delta function. This approach has been successfully applied by Fadlun [14] to study the flow past a backward facing step and by Defoe [15], who modelled a rotor blade and predicted noise propagation under the influence of inlet flow distortion.

The IBMSG method is, on the other hand, typically used to model the force field generated by a set of rotating blades. This approach assumes an infinite number of blades in the circumferential direction; which avoids the computational overhead of capturing the detailed blade geometry and/or incorporating moving boundaries in order to represent the fan. In this approach, an inviscid (or wall-normal) force and a viscous (or wall-parallel) force due to the rotating blades are added to the circumferentially averaged Navier–Stokes equations.

This method has various different forms. Marble [16] was the first to apply simple inviscid forces to ensures that the flow follows the blade metal angle. Following this concept, Chima [17] developed a model with detailed blade geometries and used this to study compressor stability. More complex models that captured detailed flow physics were then proposed and applied to a range of steady or unsteady flow simulation problems [18, 19] and stability analyseis [20] for turbomachinery. Among these, Gong [18] clarified that body forces could be separated into normal and parallel parts with the former related to the total pressure rise via a momentum equation and the latter modelled by a typical force–velocity relation. In his research, the response of a transonic compressor to inlet distortions was well captured using this model. To ensure good accuracy, the modelling of the parallel force or loss effect is also a key issue. Xu [21] introduced a loss model using a force–velocity relation, which accounts for the losses encountered over the blades. It was found that this simple relation performs well when characterising the distortion transfer in a high- pressure turbine. Compared to the mesh-resolving method, the computational cost of the simulation could be reduced by two orders of magnitude. Cao [22] and Watson [23] further developed this viscous force model by considering the effects of the casing and hub. This model showed good agreement with experiments in the study of intake distortion. However, it should be noted that this viscous body force cannot model the effect of viscosity, which tends to deviate the flow, particularly at a high incident angle.

In this paper, a mixed-fidelity approach is applied to accurately model and investigate the influence of the fan on the inlet distortion with affordable computational expense. The standard IBM proposed by Peskin [13] is used to model the distortion generator upstream of the fan. Further downstream, the IBMSG method is used to model the force field due to the rotating fan. The recovery of distortion in the presence of a fan is examined using both the mean and turbulence characteristics.

II. Numerical Framework

A. Parameters and settings

The test case considered in this study is motivated by experimental studies on the Darmstadt Rotor [24–28], In these studies, the distortion generators were designed to reproduce the flow conditions in a real engine within the laboratory. Measurements by Lieser [24] and Bitter [27] show that the compressor performance is highly sensitive to the distortions encountered at the tip. Hence, a periodic distortion generator is placed upstream of the tip of the fan in order to reproduce the distortion encountered over the intake lip at high angles of attack. Figure 1 illustrates the computational domain and the boundary conditions considered.

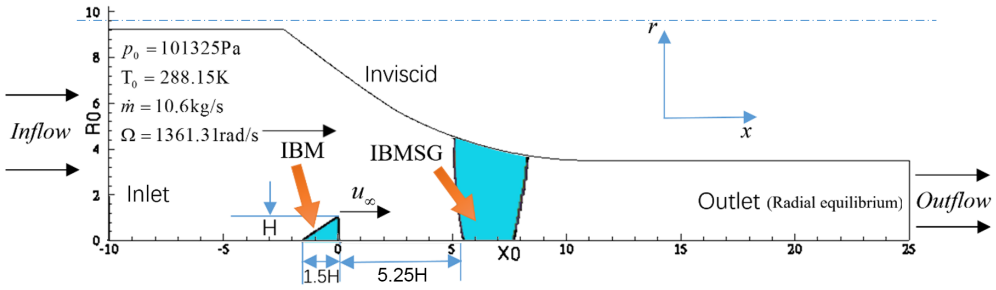

Fig. 1 Experiment settings

The test case employs the original duct and the rotating fan from Bitter's test rig set-up [27, 28], with a periodic beam installed upstream of the fan. It features a 30° sector duct with a beam height of 'H = 0.02m' and length '1.5H' placed at an axial distance of '12.5H' from the inlet. The fan is positioned at a streamwise distance of '5.25H' from the beam. All of the spatial quantities mentioned in the following sections are non-dimensionalised by the beam height H. The velocity is normalised by the velocity, u_∞, which corresponds to the outer edge velocity of the separated shear layer measured at the maximum height of the beam (Fig.1). The Reynolds number is defined based on H and u_∞, $Re = \frac{\rho u_\infty H}{\mu}$, yielding $Re \approx 1.6 \times 10^5$.

The primary objective of the current study is to capture the distortion generated on the lower wall. Hence, an inviscid boundary condition is imposed on the upper wall, which ensures that the pressure distribution due to the spinner is well represented at a reduced computational cost. International Standard Metric Conditions (P_0=101325 Pa and T_0=288.15 K) at sea level are applied at the inflow. The flow has also been tripped at an axial location of $x = -6H$ in order to ensure that a turbulent boundary layer develops upstream of the distortion generator. The mass flow rate is fixed at 10.6 kg/s, corresponding to the peak efficiency point at 65% of the rotational speed (1361.31 rad/s). A radial equilibrium boundary condition is imposed at the outflow for the test case in which the effect of fan is considered. In contrast to the full annulus considered in the experimental campaign on the Darmstadt rotor, we consider a 30° sector in the current numerical study. Periodicity is imposed in the circumferential direction. According to Tucker [29], who determined the

appropriate scale of the mesh in the spanwise direction for a wall-resolved LES, the extent of the sector (30° corresponds to $5H$ at the casing) is sufficient to ensure that the structures are decorrelated in the circumferential direction.

B. Numerical approach

The present simulations are carried out using the Rolls-Royce's in-house CFD code, HYDRA [30, 31]. No additional subgrid-scale model has been employed. Hence, the simulations can be classified as implicit LES [32]. In a mixed-fidelity framework, the beam is represented using the conventional IBM [13]. This method is also convenient for investigating the effect of the height of the distortion generators [33], as it can significantly reduce the meshing time and the mesh size to certain extent. The separated flow downstream of the beam is captured using the eddy resolving approach, while the force field of the rotating fan is modelled using the IBMSG method [22]). This approach avoids the need to resolve the detailed blade geometry or to incorporate moving boundaries. Instead, it uses the force field generated by the rotating fan blades to capture the suction effect of the fan, thereby substantially reducing the computational cost.

1. Standard IBM for beam

The distortion generator upstream of the fan is modelled using the approach of Goldstein et al. [34]:

$$\begin{aligned} \boldsymbol{f}(\boldsymbol{x},t) &= \alpha \int_0^t \Delta\boldsymbol{u}\, dt + \beta\Delta\boldsymbol{u}, \\ \Delta\boldsymbol{u} &= \boldsymbol{u}(\boldsymbol{x}_s,t) - \boldsymbol{u}_s(\boldsymbol{x}_s,t), \end{aligned} \tag{1}$$

Here, the subscript s represents the solid boundary. Coefficients α and β are negative constants, evaluated as a function of $\Delta\boldsymbol{u}$, which represents the difference between the local flow velocity and the target velocity. The target velocity is set to zero for the distortion generator. From the viewpoint of control theory, Equation 5 acts as a proportional-integral (PI) feedback controller. The 'error' $\Delta\boldsymbol{u}$ will induce the body forces to minimise this difference. It should be noted that once the solution converges to the target velocity distribution, the body force is independent of α and β. The coefficients should however be carefully selected in order to speed up convergence while maintaining stability. α and β are in fact associated with two important parameters: the frequency of the integral part of the feedback forcing, $\frac{1}{2\pi}\sqrt{|\alpha|}$, and the damping factor of the proportional part of the feedback forcing, $-\frac{\beta}{2\sqrt{|\alpha|}}$. Hence, α must be large enough to ensure that the frequency, $\frac{1}{2\pi}\sqrt{|\alpha|}$, is much larger than any other frequency within the flow [14]. This suggests that the feedback force should evolve as rapidly as possible and direct the flow to the target velocity distribution. In the current study, α and β are both set to 2.0. Waston et al. [35] verified that for both the steady and unsteady cases, the values of the coefficients α and β do not alter the converged flow field as '$\Delta\boldsymbol{u}$' approaches zero on convergence. Both the final flow field and the convergence speed were substantially independent of a range of values (0.1–10) of α and β in this study.

The time step is also bounded by the following inequality in order to ensure numerical stability:

$$\Delta t < \frac{-\beta - \sqrt{\beta^2 - 2\alpha k}}{\alpha}, \tag{2}$$

where k is a problem-dependent constant of order 1, as proposed by Goldstein [34].

2. IBMSG approach for fan modelling

The fan is represented using the IBM for 'Smeared Geometries' (IBMSG) approach which assumes that a rotating fan can be modelled as an infinite number of infinitesimally thin blades. The forces are circumferentially averaged in every cell within the region bounded by the blades, which locally turn the flow in the desired direction of the blade camber line. Cao et al. [22] introduced this method to study intake separation and demonstrated its capability in capturing the key flow features. In this model, the local force acting normal to the camber line of the blade, f_n, is again governed by Equation 5. However, the force parallel to the blade, f_p, is modelled by a typical force–velocity relation $f_p \propto \rho \boldsymbol{u}^2$ as proposed by Xu [21]. Here, ρ, $\boldsymbol{u}$ and f_p are the local density, velocity and viscous body force acting parallel to the blade camber line, respectively. The proportionality constant is generally estimated from a steady RANS simulation. Xu employed this simple relation to study three-dimensional unsteady flows and demonstrated the capability of the model to provide good estimates of the overall unsteady blade forces due to blade–row interactions. Cao [22] and Watson [23] adopted this approach to study inlet distortion transfer through the NASA and Darmstadt rotors, respectively. The same approach to the parallel force is employed in the current study:

$$\boldsymbol{f}_p = -K(r)\rho \boldsymbol{u}_{rel}^2, K(r) = 4k_1 s^2 + k_1, \tag{3}$$

where s is the fraction of span and the coefficient k_1 is a calibration constant set to 0.2 *. The finite blade thickness introduces additional blockage to the flow passing through the passage. This effect is modelled as:

$$\lambda = 1 - \frac{1}{2}\frac{(t_1 + t_2)}{S(r)\cos\beta}, \tag{4}$$

where $S(r)$ is the surface pitch and $t_1 + t_2$ is the total blade thickness (which is based on the intersection of the normal to the camber line with the blade) as shown in Figure 2. Both the normal and parallel forces are added to the compressible Navier–Stokes equations according to

$$\frac{\partial}{\partial t}\int_\Omega \lambda \mathbf{q} d\Omega + \oint_A \lambda \mathbf{G} \cdot d\boldsymbol{A} = \int_\Omega \lambda \mathbf{F} d\Omega + \int_\Omega \mathbf{S} d\Omega, \tag{5}$$

*This value is obtained by calibrating the characteristic map against the experimental and/or resolved blade data at the design speed.

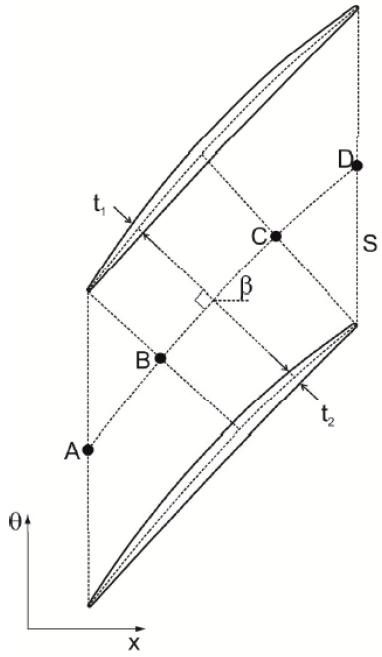

Fig. 2 Sketch of blade blockage [22]

where

$$\mathbf{q} = \begin{pmatrix} \rho \\ \rho v_x \\ \rho v_y \\ \rho v_z \\ \rho E \end{pmatrix}, \mathbf{G} = \begin{pmatrix} \rho \boldsymbol{v} \\ \rho v_x \boldsymbol{v} + p \boldsymbol{n}_x \\ \rho v_y \boldsymbol{v} + p \boldsymbol{n}_y \\ \rho v_z \boldsymbol{v} + p \boldsymbol{n}_z \\ \rho H_e \boldsymbol{v} \end{pmatrix}, \mathbf{F} = \begin{pmatrix} 0 \\ f_x + f_{p,x} \\ f_y + f_{p,y} \\ f_z + f_{p,z} \\ (\boldsymbol{f} + \boldsymbol{f_p}) \cdot \boldsymbol{v} \end{pmatrix}, \mathbf{S} = \begin{pmatrix} 0 \\ p \frac{\partial \lambda}{\partial x} \\ p \frac{\partial \lambda}{\partial y} \\ p \frac{\partial \lambda}{\partial z} \\ 0 \end{pmatrix}. \tag{6}$$

C. Mesh quality

Table 1 provides the details of the grids used in the current study. Around 60 M mesh nodes are used for the fine mesh. Streamwise, pitchwise and spanwise distributions of the nodes in the region of interest (beam, recirculation zone and fan) are also tabulated. For the fine mesh, the grid resolution is within the wall units of $\Delta x^+ = 50 \sim 130$, $\Delta y^+ = 1$ and $\Delta z^+ = 15 \sim 30$, which are the wall spacing requirements recommended by Tucker [36]).

Following You [37], the grid resolution within the shear layer downstream of the beam is estimated in Kolmogorov units as follows:

$$R = \frac{V^{1/3}}{\eta}, \eta = \left(\frac{\nu^3}{\varepsilon}\right)^{1/4}. \tag{7}$$

Here V is the cell volume and η is the Kolmogorov length scale. The dissipation in the above equation is approximated by $\varepsilon = \mathcal{P} - C$, where $\mathcal{P}$ and C are the production and convection of turbulent kinetic energy, respectively. Figure 3a

Table 1 Grid distribution

Grid size	Δx^+	Δy^+	Δz^+	Number of nodes
Fine mesh	75	1	30	59,371,200
Coarse mesh	150	1	100	8,600,100
Region nodes	streamwise	pitchwise	spanwise	Total nodes
Beam	60	100	400	2,400,000
Recirculation	250	150	400	15,000,000
Fan	120	193	400	9,264,200
Total	776	193	400	59,371,200

shows the distribution of the ratio R in the recirculation zone. The values of R are within a value of 50, which meet the resolution requirement proposed by You [37], except for a very small area at the beginning of shear layer, which does not affect the main area of the simulation. Figure 3b also shows the auto-correlation of u' at three different points (marked in Fig. 3a). The auto-correlation crosses zero at around 4°, indicating that a spanwise extent of 30° is large enough to accommodate all of the modes along the span.

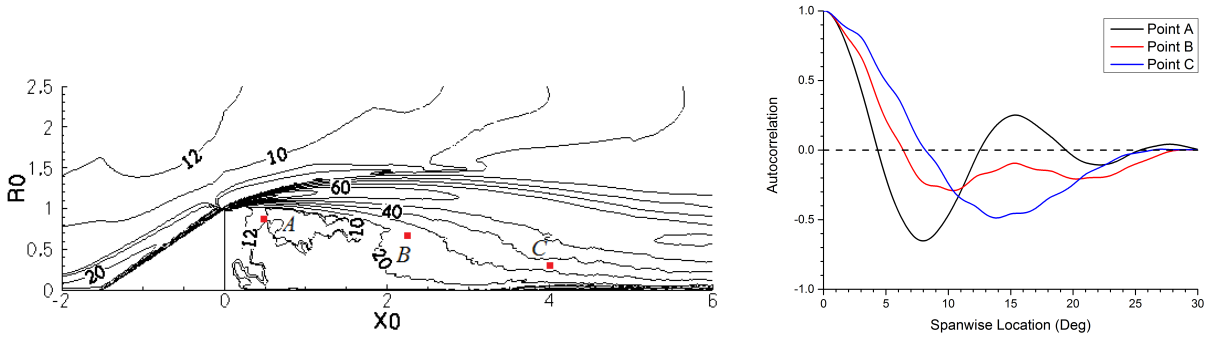

(a) Resolution in Komogorov units (η) **(b) Auto-correlations for Point A/B/C**

Fig. 3 Mesh quality

In order to estimate the sensitivity of the findings to the grid resolution, studies are also carried out on a coarser mesh which consists of ≈ 9 M ($\times 10^6$) mesh nodes. Figure 4 shows the distributions of the mass flow rate and pressure at $x = 4.5H$ for the case with the fan. Consistent results are observed on both the grids, thereby demonstrating that the results presented here are mesh independent.

III. Validation of IBM

Watson et al. [35] validated the IBMSG approach using RANS for a range of cases. This included a compressor blade row, a high ratio fan stage and the Darmstadt rotor, and showed that the model is very effective in predicting the general fan behaviour. The IBM for flows at high Reynolds numbers was also validated by Iaccarino et al. [38]. Despite

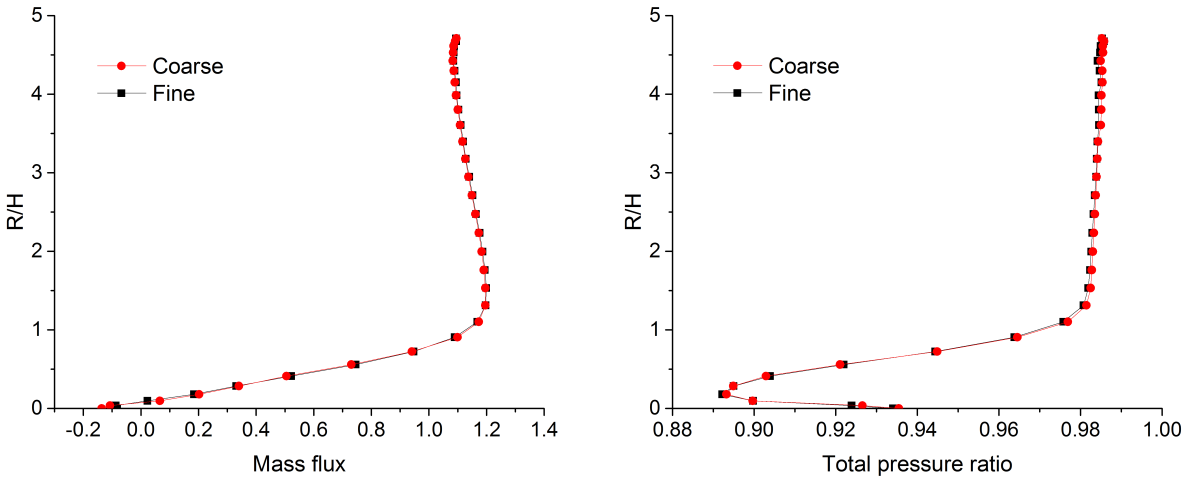

(a) Mass flux distribution **(b) Total pressure distribution**

Fig. 4 Flow distribution of LES cases with different grid size at $x = 4.5H$(time averaged, with fan)

this, a rare validation using the IBM for second-order turbulence statistics has been conducted. Hence, in this section, high-fidelity turbulence modelling with the IBM is tested on the flow around a triangular prism with an apex angle of 60°. This flow has been studied by Agrwal [39], who used Particle Image Velocimetry (PIV), hotwire anemometry and flow visualisation techniques to measure the velocity field. Likewise, we conducted a numerical study for the same test but used the Large Eddy Simulation (LES) method with an IBM to model the triangular prism. The original prism for the experiment has an equilateral triangular cross-section, with sides of length D=6 mm and a length of $6D$ in the spanwise direction. The inlet velocity is around 1 m/s, and the Reynolds number is set to 520. For the present numerical simulation, in order to use the compressible code, the test case is scaled down by 150:1, and the inlet velocity is also adjusted to $Ma = 0.35$, which guarantees the same Reynolds number as the experiment. The computational region is extended to $10D$ in the streamwise and pitchwise directions, with 150 grid points for each. In the spanwise direction, 100 grid points are allocated. In total, around 2.25 million cells are deployed in the computational domain. Two calculations have been performed, one with an IBM modelled prism and the other with a mesh resolved prism. Implicit LES is used for both cases. Around 20 flow throughs are used to collect the mean flow and statistics).

Figure 5 shows the distributions of axial velocity (normalised by inlet velocity U_0) of the potential flow in the y direction at points $x = 2D$ and $x = 4D$. Corresponding contours of the second-order statistics of turbulence intensity and TKE production are also shown in Figures 6 and 7 respectively (spanwise averaged). The results obtained from IBM, fully resolved geometry and measurements are compared in these figures. The predictions from IBM are in favourable agreement with those from the fully resolved geometry. The velocity profiles from the experiment show a certain degree of asymmetry while the numerical results are much more symmetric. Although marginal deviations in the regions of high shear are observable, the predictions are largely in line with the experimental results, thus validating the IBM

framework.

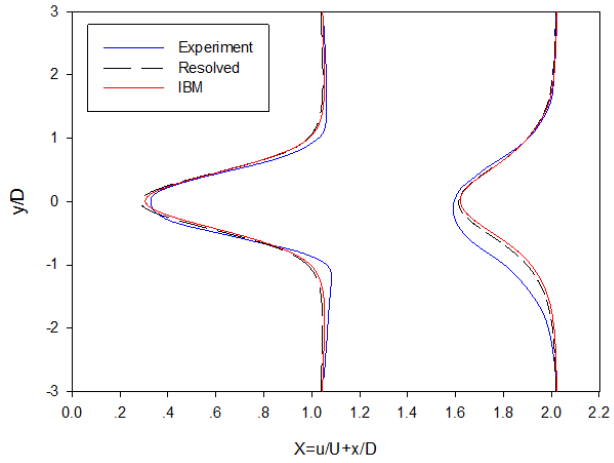

Fig. 5 Distribution of axial velocity at $x = 2D/4D$

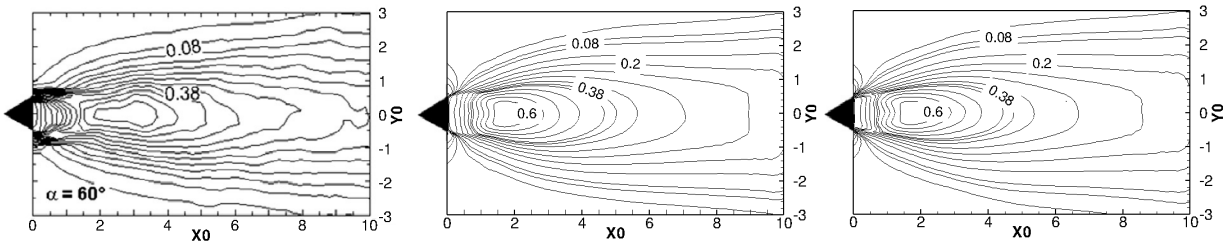

Fig. 6 Contours of turbulence intensity (from left to right: experiment[39]/resolved/IBM modelled)

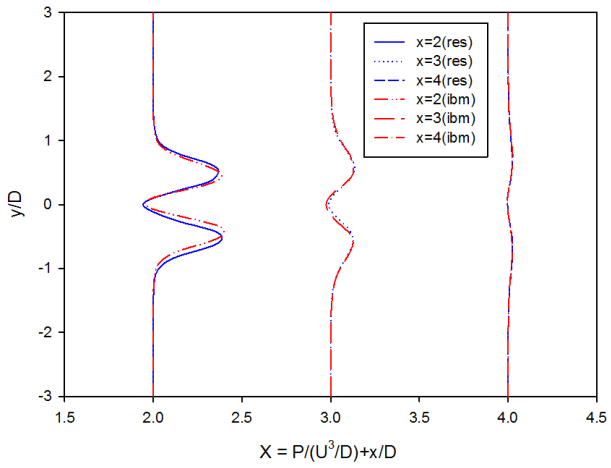

Fig. 7 Distribution of TKE Production at x=2D/3D/4D

IV. The influence of fan on inlet distortion

In this section the effect of fan on both the instantaneous and time-mean flow field will be discussed. Comparisons will be drawn against the clean case in the absence of a fan.

A. Instantaneous flow field

In order to qualitatively verify that both the IBM and IBMSG models behave as expected, Figure 8 shows the contours of the stagnation pressure of the instantaneous flow. This demonstrates both the distortion generated in the lee of the beam and the increase in the stagnation pressure due the presence of the fan. n increase in the stagnation pressure due the presence of the fan.

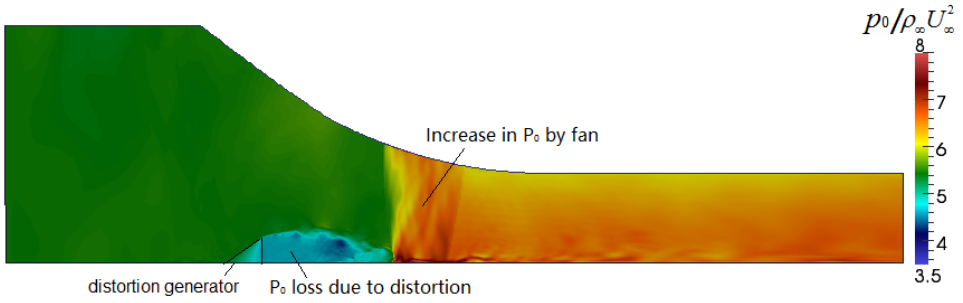

Fig. 8 Total pressure distribution of the instantaneous flow

The iso-surfaces of Q-criterion (Q=40) in different views are illustrated in Figure 9a and 9b, contoured with the local axial velocity ($v_x = -150 \sim 200$). The axial location of the fan is also shown by means of a sketch. A coherent two-dimensional detached shear layer forms at the edge of the beam, which rapidly destabilises downstream. A decrease in scale of the recirculation region is clearly evident in the presence of the fan. Qualitatively, in the subfigure (located in the top-left corner) in Fig. 9b, an increase in the length scales of the turbulent structures due to the fan is notable. Quantitative estimates of the change in the lengths scales can be obtained from the two-point correlations. This requires saving long time-series data however, which is beyond the scope of the current work.

B. Time averaged flow field

Time integration is carried out using an explicit 5-stage Runge–Kutta time-stepping scheme [40]. After flushing out the initial transience, time averaging (running average) of the primitive variables and high-order statistics (Reynolds stresses) has been carried out for around $150H/U_\infty$ time units. The maximum deviation of $\langle u'u' \rangle$ is less than 1%, when the flow field is further averaged for $50H/U_\infty$ time units, indicating that the convergence is acceptable. Figure 10 compares the mean velocity profiles at different streamwise locations on a carpet plot. A line joining the locus of inflectional points of the velocity profiles is also overlaid on this plot. As noted from the instantaneous flow, the extent of the recirculation zone has significantly reduced due to the fan. The flow reattaches at an axial location which is more

Fig. 9 Iso-surfaces of Q-criterion in different views

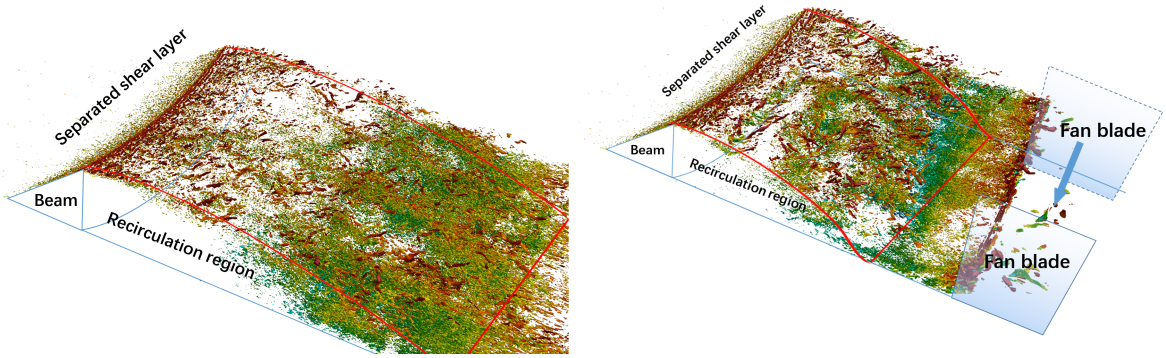

(a) Instantaneous flow for the cases without/with fan

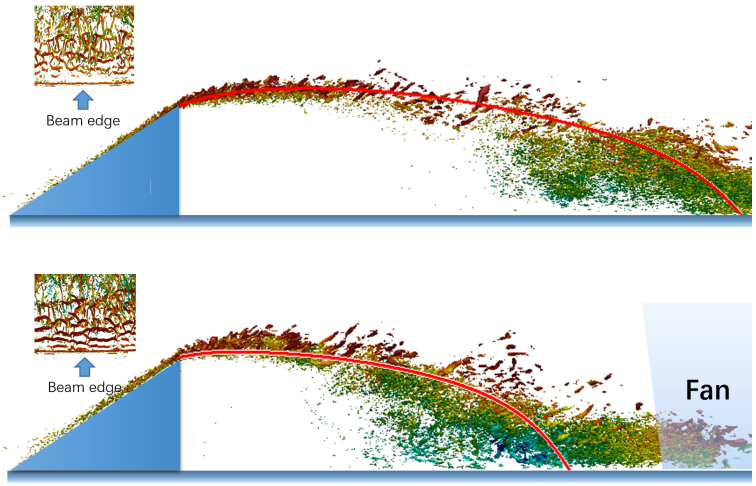

(b) Lateral view of instantaneous flow for the cases without/with fan

than a beam height upstream of the fan leading edge.

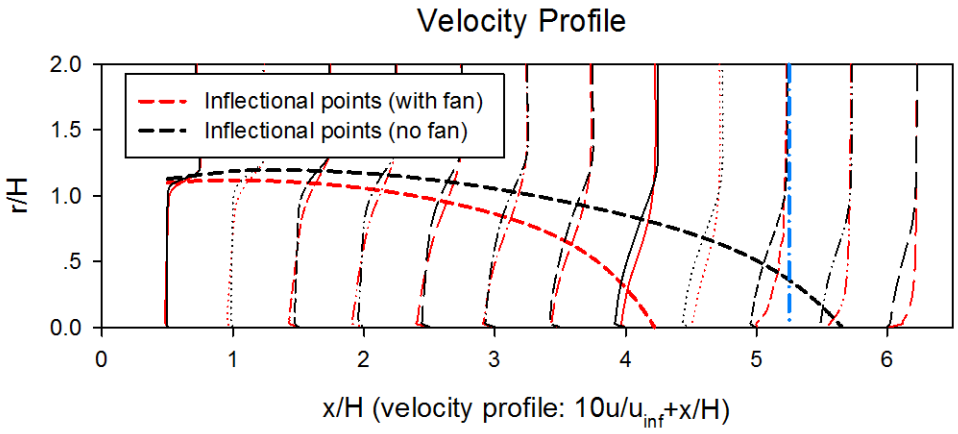

Fig. 10 Velocity profile at different streamwise locations (The blue dash-dotted line denotes the leading edge of the fan)

Figure 11a shows the contours of the time-averaged turbulent kinetic energy. The TKE values in the shear layer and in the reattaching regime have increased by around 40% to 70% in the axial direction in the presence of the fan. A local maximum in the TKE production at the leading edge of the blade tip is notable. This local TKE has a minimal effect on the size of the separation bubble when compared to that of the potential field and the mass-flow redistribution. This aspect has been ensured by considering different fan designs.

To reveal the role of the fan in the balance of the turbulent kinetic energy, the convection and production terms are investigated in detail here. Equation 8 presents all of the relevant terms.

$$\frac{\partial k}{\partial t} = \underbrace{-\overline{u_i' u_j'}\frac{\partial \overline{u_i}}{\partial x_j}}_{\text{Production } \mathcal{P}} \underbrace{-\overline{u_j}\frac{\partial k}{\partial x_j}}_{\text{Convection } C} - \frac{1}{\rho}\frac{\partial \overline{u_j' p'}}{\partial x_j} - \frac{\partial \overline{u_j' u_i' u_i'}}{\partial x_j} + \nu\frac{\partial^2 k}{\partial x_j^2} - \nu\overline{\left(\frac{\partial u_i'}{\partial x_j}\right)^2}, \tag{8}$$

where the fluctuation of body force caused by gravity is neglected. A higher production in the shear layer is evident in Figure 11b. This could be the main source of the increased turbulent kinetic energy. Figure 11c illustrates the distribution of the TKE convection, showing a massive intensification of convection caused by the fan.

V. Mechanism

A. Turbulence statistics

This section details the mechanism by which the fan reduces the scale of the recirculation region. In the previous section, Figure 11b and 11c demonstrate a substantial increase in both production and convection. However, the location of the increase varies, and consequently may present different traits. To examine this in more detail, the relevant

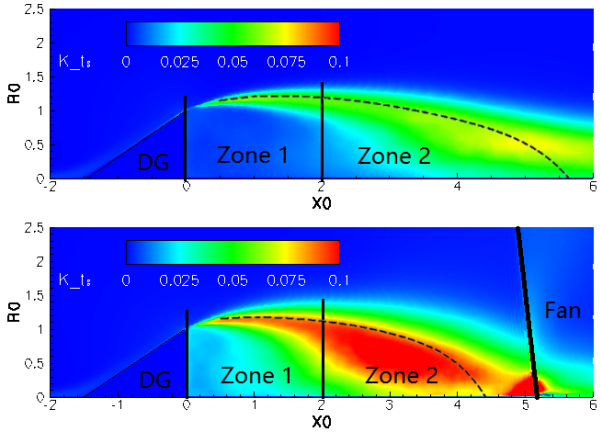

(a) Contours of TKE

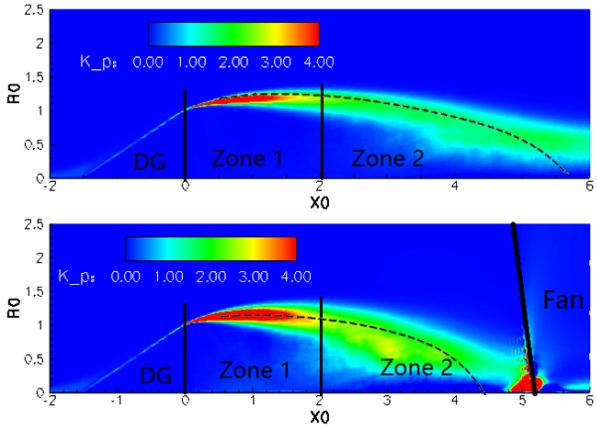

(b) Contours of TKE Production

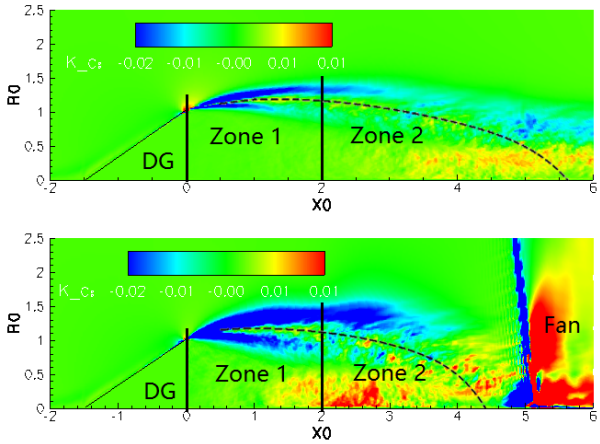

(c) Contours of TKE convection

Fig. 11 Turbulent Kinetic Energy Statistics

turbulence statistics are analysed in the individual Zones. This includes the TKE production and convection, and the relevant dominant Reynolds stresses and velocity gradients.

The results demonstrate that there are two distinct mechanisms through which the fan affects the separated flow: a shear flow dominant zone (Zone 1) and a streamline curvature dominant zone (Zone 2). Figures 12a and 12b show that in Zone 2, the primary effect of the fan is observable between $x = 2H$ and $4H$ where the recirculation region decreases due to the change of the streamline curvature, which essentially results from the change of the potential field upstream of the fan. Both $\langle u'u' \rangle$ and $\langle v'v' \rangle$ increase significantly within this region by approximately 40% and 75%, respectively. The increase in $\langle v'v' \rangle$ is much more pronounced than $\langle u'u' \rangle$, indicating a stronger turbulent transport in the wall-normal direction. This is similar to what is observed in the context of corner separation [41] at the leading edge of blade and is also consistent with the observations of Bradshaw [42]. Hence, we consider this increase in the Reynolds stresses to be a 'direct effect' of the additional strain rate caused by the curvature change.

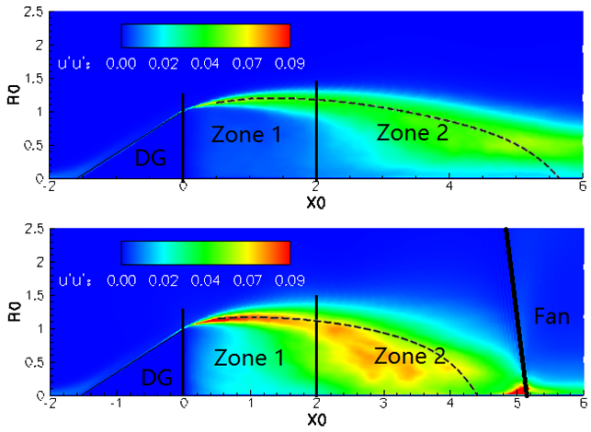

(a) Reynolds stress $\langle u'u' \rangle$

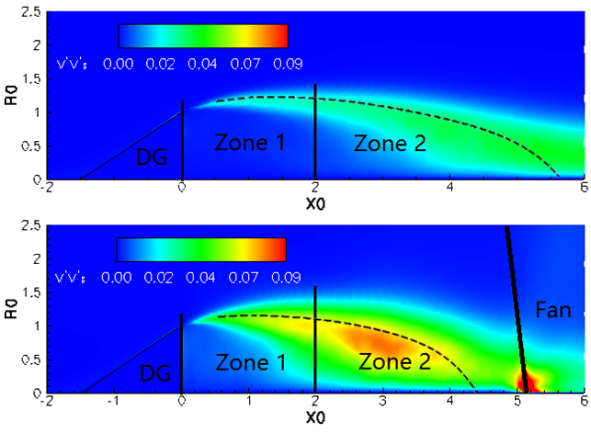

(b) Reynolds stress $\langle v'v' \rangle$

Fig. 12 Main Reynolds stresses

The increased turbulence in Zone 2 also influences the flow in Zone 1, and is revealed by the TKE convection. In Figure 11c, the blue area indicates negative convection and the red positive convection. Hence, the dominant term of convection $-\overline{u}\dfrac{\partial k}{\partial x}$ in the upper part of recirculation region in Zone 2 is negative, and thus $\dfrac{\partial k}{\partial x}$ is positive, indicating that the TKE increases along the streamwise direction. Conversely, in the lower part, the TKE increases towards the negative x-direction. This means that the TKE is convected with the recirculating flow, and transported back to Zone 1. When the fan is installed, this convection process is greatly intensified. Consequently, we may conclude that the turbulence from the vicinity of the fan feeds back into the origin of the shear layer by means of the recirculating flow.

In Zone 1, the enhanced turbulence due to the convection further intensifies the shear layer. As expected, $\langle u'v' \rangle (\partial U/\partial y)$ is found to be the major contributor to the total production of TKE in Zone 1 within the spreading shear layer. Figure 13 compares the velocity gradients $\partial U/\partial y$ to the contours of the Reynolds stress $\langle u'v' \rangle$ without/with fan. It is evident that the contribution to the TKE production is primarily affected by an increase in the Reynolds stress $\langle u'v' \rangle$, while the change in the velocity gradients is marginal. (The relative change of $\langle u'v' \rangle$ is nearly 6 times that of $\partial U/\partial y$ within both the shear layer and Zone 2.) Figures 12a and 12b also demonstrate an increase in both the streamwise and wall-normal fluctuations within the shear layer at the edge of the beam between $x = 0$ and $2H$. Clearly, the spreading rate of the shear layer is higher in the presence of the fan.

Again, the increased TKE in Zone 1 is subsequently convected downstream into Zone 2 through the mainstream flow and results in cyclic feedback between the zones. Hence, although the flow in Zone 1 is not affected directly by the fan, it is still a key source of turbulence due to the feedback from the reverse flow. It supplements the turbulence generated in the vicinity of the fan in Zone 2 and also contributes to the earlier reattachment of the separation bubble.

B. Turbulence structure

Here, we further look into the turbulence structure to understand the fan effect. The Barycentric map [43] is used to capture the turbulence anisotropy in the spatial domain. This is quantified by the normalised Reynolds stress anisotropy tensor

$$a_{ij} = \frac{\langle u_j u_j \rangle}{2k} - \frac{\delta_{ij}}{3} \tag{9}$$

where $k = \langle u_i u_i \rangle /2$. The eigenvalues λ_1, λ_2 and λ_3 ($\lambda_1 > \lambda_2 > \lambda_3$) of this asymmetric tensor then form three important coefficients

$$\begin{cases} C_{1c} = \lambda_1 - \lambda_2 \\ C_{2c} = 2(\lambda_2 - \lambda_3) \\ C_{3c} = 3\lambda_3 + 1 \end{cases} \tag{10}$$

According to Banerjee et al. [43], these three coefficients capture the 1-component, 2-component and 3-component (or isotropy) states of the turbulence, respectively. Accordingly, Emory et al. [44] proposed that the RGB colouring system

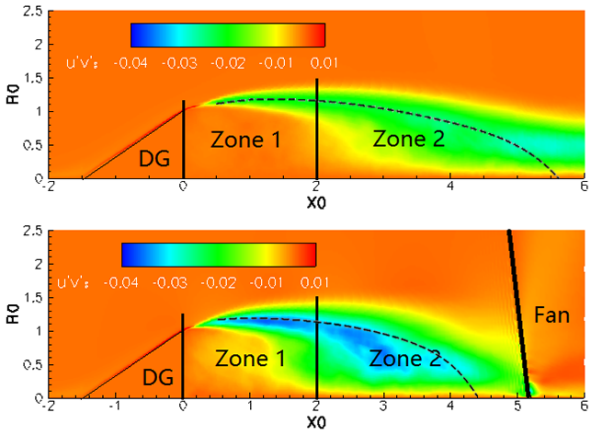

(a) Reynolds stress $\langle u'v' \rangle$

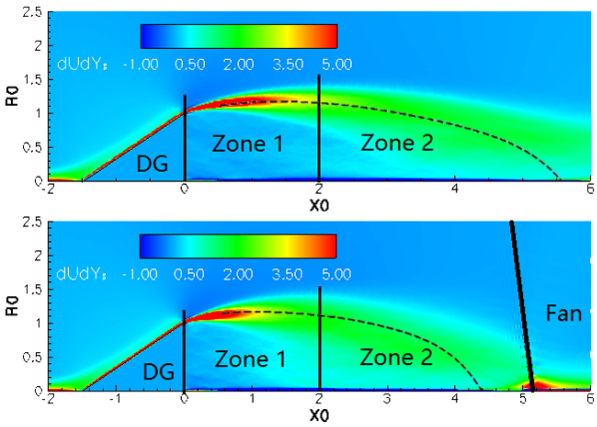

(b) Velocity gradient $\partial U/\partial y$

Fig. 13 Terms of TKE Production $\langle u'v' \rangle \, \partial U/\partial y$

can be applied to illustrate this turbulence componentality in the spatial domain. Here the RGB value can be formulated as

$$\begin{bmatrix} R \\ G \\ B \end{bmatrix} = C_{1c} \begin{bmatrix} 1 \\ 0 \\ 0 \end{bmatrix} + C_{2c} \begin{bmatrix} 0 \\ 1 \\ 0 \end{bmatrix} + C_{3c} \begin{bmatrix} 0 \\ 0 \\ 1 \end{bmatrix}. \tag{11}$$

Hence, each point within the flow field has a corresponding RGB value which represents the anisotropy associated with the turbulent flow. The anisotropy componentality contours of the separation region for the two cases are depicted in Figure 15.

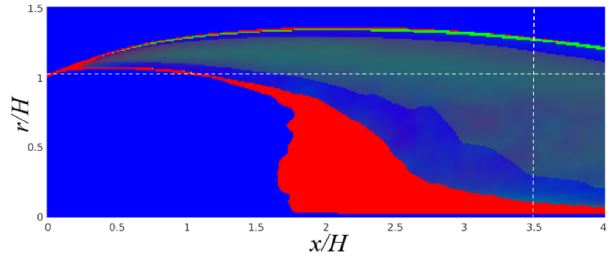

(a) No fan

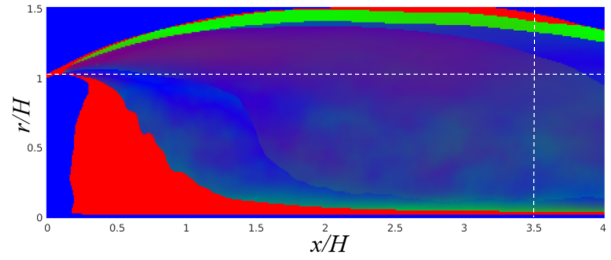

(b) With fan

Fig. 14 Anisotropy componentality contours: red: one-component, green: two-components, blue: isotropic

Frame (a) shows that inside the bubble, the turbulence is of mainly 2 and 3-component form (coloured in green and blue). When the fan is installed (Frame (b)), the flow reattaches earlier and the recirculation region becomes bluer, meaning the turbulence becomes more isotropic. This indicates that the fan can redistribute the anisotropy within the separation bubble. In the vicinity of the fan (Zone 2), it is the direct effect we discussed previously that moves the 1-component turbulence dominant region (coloured in red) towards the beam.

To quantify this trend to isotropy, and show such variation, two variables are defined according to [43]. These are

$$x_B = C_{1c} + \frac{1}{2} C_{3c}, y_B = \frac{\sqrt{3}}{2} C_{3c}. \tag{12}$$

Hence, this coordinate system defines a Barycentric map, and three limiting states, 1/2/3 components $X_1 = (1, 0), X_2 =$

$(0, 0)$, $X_3 = (1/2, \sqrt{3}/2)$, can be fixed at the three vertices of the equilateral triangle on the map (Fig. 15a). For the present case, two positions are chosen to show the trajectories of the anisotropy variations. They are extracted along the lines marked in Figure 14: $r = H$ (along the shear layer) and $x = 3.5H$ (across the shear layer). Frame 15a shows that, along the shear layer, the region defined by $x = H - 4H$ is significantly more isotropic due to the presence of the fan. Similarly, in the radial direction, Frame 15b also illustrates that the turbulence tends to be more isotropic within the recirculation region ($r = 0.3H - 1.2H$). This demonstrates that the fan weakens anisotropy specifically during the flow reattachment within in the recovering wake region. This is attributed to the following factors: a) the early reattachment process promoted by the fan (also noted by Alam and Sandham [45] and Vadlamani [46]) and b) the adverse pressure gradient experienced by the flow as it approaches the fan. Both of these factors contribute to the effective redistribution of turbulence, promoting isotropy. However, Figure 14 also shows that in the majority of the recirculation region, the turbulence still shows strong anisotropy: near 1-component within the shear layer and mixed components in the rest of the area. This is consistent with the findings of [46] and [47] in the context of separation induced due to adverse pressure gradients and separation from a rounded step respectively. Unlike the eddy-resolving simulations (LES/DNS), the RANS models using isotropic turbulence could hence be inaccurate in predicting such regions to have strong anisotropy.

We may further deduce that the anisotropy redistribution caused by the fan could have three benefits. Since isotropic turbulence is always homogeneous by definition, the gradient of the mean variables of the potential flow is diminished [48]. As a result, the distortion in front of the fan is alleviated. The other two benefits relate to the increased turbulence level. The turbulence can be much more easily diffused in all directions by more isotropic turbulence. Hence, the mixing process between the recirculated flow and the mean flow can be enhanced, leading to an earlier reattachment. In addition, the increased energy generated from the shear layer can be also be quickly dissipated by such fully developed turbulence. Consequently, the energy of the distorted flow will decrease and the distortion will be alleviated.

VI. Conclusion

In this paper, we proposed a mixed-fidelity approach to study the influence of a fan on inlet distortion at an affordable computational cost. The validation of the IBM indicates that the present method can predict both the potential flow quantities and turbulence statistics accurately. Hence, this method can be used to replace the resolved distortion generator and to investigate the influence of the fan on the distortion.

The second test case demonstrates that there are two mechanisms through which the fan affects the separated flow: Firstly, the suction effect of the fan (effective up to almost half of the chord length upstream of the fan) accelerates the flow in the intake and changes the streamline curvature. This change closes the recirculation bubble much earlier and alleviates the undesired distortion 'directly'. However, the acceleration due to the suction effect is not sufficient to relaminarise the flow (acceleration parameter, $K \sim 10^{-6}$ [49]). In contrast, the adverse pressure gradient caused by the fan also increases the production of turbulence near the fan leading edge. Secondly, within the recirculation region, the

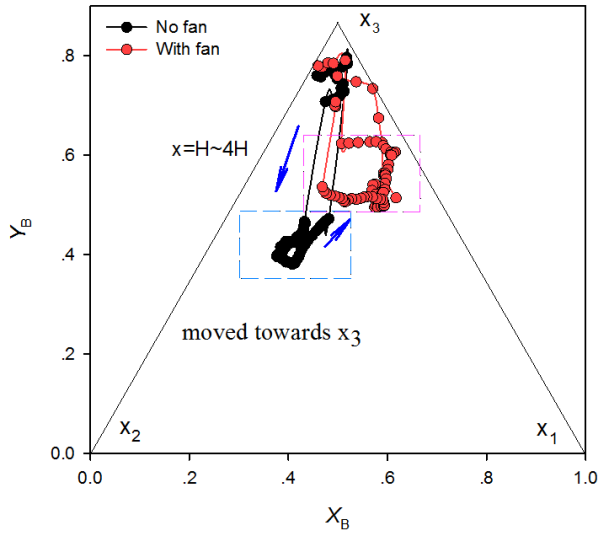

(a) $r = H$

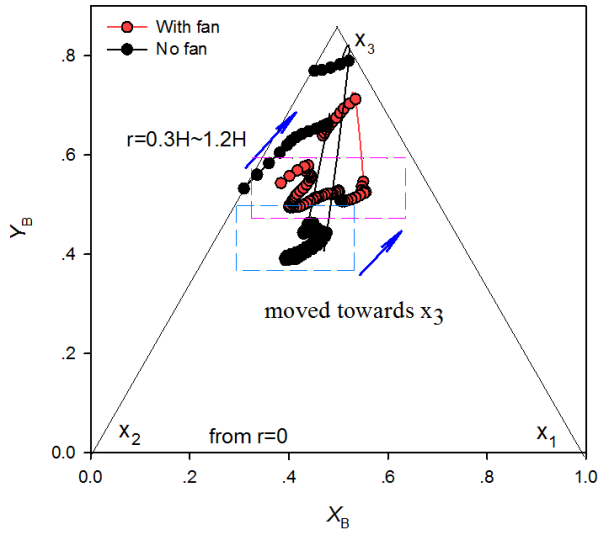

(b) $x = 0.5H$

Fig. 15 Barycentric maps

strain rate and turbulence transport are intensified. The enhanced turbulence in the vicinity of the fan feeds back into the initial growth of the shear layer by means of the recirculating flow. This 'indirect' feedback is found to increase the turbulence production and the spreading rate of the shear layer. Both these direct and indirect effects of the fan significantly suppress the inlet distortion.

Acknowledgments

The authors acknowledge the computing time on the UK national high-performance computing service ARCHER provided via the UK Turbulence Consortium in the framework of the EPSRC grant EP/L000261/1. This work is funded by a studentship from the Chinese Scholarship Council. The code for this project is provided by the Rolls-Royce plc. All the funding and technical support from these organisations are gratefully acknowledged.

References

[1] Cao, T., Vadlamani, N. R., Tucker, P. G., Smith, A. R., Slaby, M., and Sheaf, C. T., "Fan–Intake Interaction Under High Incidence," *Journal of Engineering for Gas Turbines and Power*, Vol. 139, No. 4, 2017, p. 041204.

[2] Fidalgo, V. J., Hall, C., and Colin, Y., "A study of fan-distortion interaction within the nasa rotor 67 transonic stage," *Journal of Turbomachinery*, Vol. 134, No. 5, 2012, p. 051011.

[3] Barthmes, S., Haug, J. P., Lesser, A., and Niehuis, R., "Unsteady CFD simulation of transonic axial compressor stages with distorted inflow," *Advances in Simulation of Wing and Nacelle Stall*, Springer, 2016, pp. 303–321.

[4] Seddon, J., and Goldsmith, E. L., *Intake aerodynamics*, Amer Inst of Aeronautics &, 1999.

[5] Tucker, P., and Liu, Y., "Turbulence Modeling for Flows Around Convex Features," *44th AIAA Aerospace Sciences Meeting and Exhibit*, 2006, p. 716.

[6] Liu, Y., Lu, L., Fang, L., and Gao, F., "Modification of Spalart–Allmaras model with consideration of turbulence energy backscatter using velocity helicity," *Physics Letters A*, Vol. 375, No. 24, 2011, pp. 2377–2381.

[7] Gourdain, N., Gicquel, L. Y., and Collado, E., "Comparison of RANS and LES for prediction of wall heat transfer in a highly loaded turbine guide vane," *Journal of propulsion and power*, Vol. 28, No. 2, 2012, pp. 423–433.

[8] Liu, Y., Yu, X., and Liu, B., "Turbulence models assessment for large-scale tip vortices in an axial compressor rotor," *Journal of Propulsion and Power*, Vol. 24, No. 1, 2008, p. 15.

[9] Spalart, P., and Bogue, D., "The role of CFD in aerodynamics, off-design," *The Aeronautical Journal (1968)*, Vol. 107, No. 1072, 2003, pp. 323–329.

[10] Liu, Y., Yan, H., Lu, L., and Li, Q., "Investigation of Vortical Structures and Turbulence Characteristics in Corner Separation in a Linear Compressor Cascade Using DDES," *Journal of Fluids Engineering*, Vol. 139, No. 2, 2017, p. 021107.

[11] Gao, F., Ma, W., Sun, J., Boudet, J., Ottavy, X., Liu, Y., Lu, L., and Shao, L., "Parameter study on numerical simulation of corner separation in LMFA-NACA65 linear compressor cascade," *Chinese Journal of Aeronautics*, Vol. 30, No. 1, 2017, pp. 15–30.

[12] Sirovich, L., "Initial and boundary value problems in dissipative gas dynamics," *The Physics of Fluids*, Vol. 10, No. 1, 1967, pp. 24–34.

[13] Peskin, C. S., "The immersed boundary method," *Acta numerica*, Vol. 11, 2002, pp. 479–517.

[14] Fadlun, E., Verzicco, R., Orlandi, P., and Mohd-Yusof, J., "Combined immersed-boundary finite-difference methods for three-dimensional complex flow simulations," *Journal of computational physics*, Vol. 161, No. 1, 2000, pp. 35–60.

[15] Defoe, J. J., and Spakovszky, Z. S., "Effects of Boundary-Layer Ingestion on the Aero-Acoustics of Transonic Fan Rotors," *Journal of Turbomachinery*, Vol. 135, No. 5, 2013, p. 051013.

[16] Marble, F. E., "Three-dimensional flow in turbomachines," *High Speed Aerodynamics and Jet Propulsion*, Vol. 10, 1964, pp. 83–166.

[17] Chima, R. V., "A three-dimensional unsteady CFD model of compressor stability," *ASME Turbo Expo 2006: Power for Land, Sea, and Air*, American Society of Mechanical Engineers, 2006, pp. 1157–1168.

[18] Gong, Y., Tan, C., Gordon, K., and Greitzer, E., "A computational model for short wavelength stall inception and development in multi-stage compressors," *ASME 1998 International Gas Turbine and Aeroengine Congress and Exhibition*, American Society of Mechanical Engineers, 1998, pp. V001T01A114–V001T01A114.

[19] Gordon, K. A., "Three-dimensional rotating stall inception and effects of rotating tip clearance asymmetry in axial compressors," Ph.D. thesis, Massachusetts Institute of Technology, 1999.

[20] Sun, X., Ma, Y., Liu, X., and Sun, D., "Flow Stability Model of Centrifugal Compressors Based on Eigenvalue Approach," *AIAA Journal*.

[21] Xu, L., "Assessing viscous body forces for unsteady calculations," *ASME Turbo Expo 2002: Power for Land, Sea, and Air*, American Society of Mechanical Engineers, 2002, pp. 323–331.

[22] Cao, T., Hield, P., and Tucker, P. G., "Hierarchical immersed boundary method with smeared geometry," *54th AIAA Aerospace Sciences Meeting*, 2016, p. 2130.

[23] Watson, R., Cui, J., Ma, Y., and Hield, P., "Improved hierarchical modelling for aerodynamically coupled systems," *ASME Turbo Expo 2017: Turbine Technical Conference and Exposition*, American Society of Mechanical Engineers, 2017.

[24] Lieser, J., Biela, C., Pixberg, C., Schiffer, H.-P., Schulze, S., Lesser, A., Kähler, C., and R, N., "Compressor Rig Test with Distorted Inflow using Distortion Generators," .

[25] Niehuis, R., Lesser, A., Probst, A., Radespiel, R., Schulze, S., Kähler, C., Spiering, F., and Kroll, N., "Simulation of nacelle stall and engine response," .

[26] Übelacker, S., Hain, R., and Kähler, C. J., "Flow Investigations in a Stalling Nacelle Inlet Under Disturbed Inflow," *Advances in Simulation of Wing and Nacelle Stall*, Springer, 2016, pp. 271–283.

[27] Bitter, M., Wartzek, F., Übelacker, S., Schiffer, H.-P., and Kähler, C. J., "Characterization of a distorted transonic compressor flow using dual-luminophore pressure-sensitive paint," *10th Pacific Symposium on Flow Visualization and Image Processing (PSFVIP-10), fedOA (Federico II Open Archive), Naples, Italy*, 2015.

[28] Wartzek, F., Holzinger, F., Brandstetter, C., and Schiffer, H.-P., "Realistic inlet distortion patterns interacting with a transonic compressor stage," *Advances in Simulation of Wing and Nacelle Stall*, Springer, 2016, pp. 285–302.

[29] Tucker, P. G., *Advanced Computational Fluid and Aerodynamics*, Vol. 54, Cambridge University Press, 2016.

[30] Crumpton, P., Moinier, P., and Giles, M., "An unstructured algorithm for high Reynolds number flows on highly stretched grids," *Numerical methods in laminar and turbulent flow*, 1997, pp. 561–572.

[31] Lapworth, L., "Hydra-CFD: a framework for collaborative CFD development," *International Conference on Scientific and Engineering Computation (IC-SEC), Singapore, June*, Vol. 30, 2004.

[32] Grinstein, F. F., Margolin, L. G., and Rider, W. J., *Implicit large eddy simulation: computing turbulent fluid dynamics*, Cambridge university press, 2007.

[33] Ma, Y., Cui, J., Vadlamani, N. R., and Tucker, P., "A mixed-fidelity numerical study for fan-distortion," *ASME Turbo Expo 2018*, American Society of Mechanical Engineers, 2018.

[34] Goldstein, D., Handler, R., and Sirovich, L., "Modeling a no-slip flow boundary with an external force field," *Journal of Computational Physics*, Vol. 105, No. 2, 1993, pp. 354–366.

[35] Watson, R., Cui, J., Ma, Y., Tyacke, J., Vadlamani, N. R., Alam, M. F., Dai, Y., Tucker, P. G., Cao, T., Hield, P., et al., "Improved Hierarchical Modelling for Aerodynamically Coupled Systems," *ASME Turbo Expo 2017: Turbomachinery Technical Conference and Exposition*, American Society of Mechanical Engineers, 2017, pp. V02BT41A056–V02BT41A056.

[36] Tucker, P., *Unsteady computational fluid dynamics in aeronautics*, Vol. 104, Springer Science & Business Media, 2013.

[37] You, D., Wang, M., Moin, P., and Mittal, R., "Large-eddy simulation analysis of mechanisms for viscous losses in a turbomachinery tip-clearance flow," *Journal of Fluid Mechanics*, Vol. 586, 2007, pp. 177–204.

[38] Iaccarino, G., and Verzicco, R., "Immersed boundary technique for turbulent flow simulations," *Applied Mechanics Reviews*, Vol. 56, No. 3, 2003, pp. 331–347.

[39] Agrwal, N., Dutta, S., and Gandhi, B., "Experimental investigation of flow field behind triangular prisms at intermediate Reynolds number with different apex angles," *Experimental Thermal and Fluid Science*, Vol. 72, 2016, pp. 97–111.

[40] Martinelli, L., "Calculations of viscous flows with a multigrid method," Tech. rep., Princeton Univ., NJ (USA), 1987.

[41] Liu, Y., Yan, H., Liu, Y., Lu, L., and Li, Q., "Numerical study of corner separation in a linear compressor cascade using various turbulence models," *Chinese Journal of Aeronautics*, Vol. 29, No. 3, 2016, pp. 639–652.

[42] Bradshaw, P., "Effects of Streamline Curvature on Turbulent Flow." Tech. rep., DTIC Document, 1973.

[43] Banerjee, S., Krahl, R., Durst, F., and Zenger, C., "Presentation of anisotropy properties of turbulence, invariants versus eigenvalue approaches," *Journal of Turbulence*, , No. 8, 2007, p. N32.

[44] Emory, M. A., "Estimating model-form uncertainty in Reynolds-averaged Navier-Stokes closures," Ph.D. thesis, 2014.

[45] Alam, M., and Sandham, N. D., "Direct numerical simulation of 'short'laminar separation bubbles with turbulent reattachment," *Journal of Fluid Mechanics*, Vol. 410, 2000, pp. 1–28.

[46] Vadlamani, N. R., "Numerical investigation of separated flows in low pressure turbines," Ph.D. thesis, University of Cambridge, 2014.

[47] Bentaleb, Y., Lardeau, S., and Leschziner, M. A., "Large-eddy simulation of turbulent boundary layer separation from a rounded step," *Journal of Turbulence*, , No. 13, 2012, p. N4.

[48] Brodkey, R. S., *The phenomena of fluid motions*, Courier Corporation, 1995.

[49] Yang, X., and Tucker, P. G., "Assessment of turbulence model performance: Severe acceleration with large integral length scales," *Computers & Fluids*, Vol. 126, 2016, pp. 181–191.

Appendix: Velocity Profiles from RANS and LES

The velocity profiles from RANS and LES are quite different for the case without fan. However, this discrepancy is minimised when the fan is installed. This indicates that the fan has substantial influence on the prediction of separation.

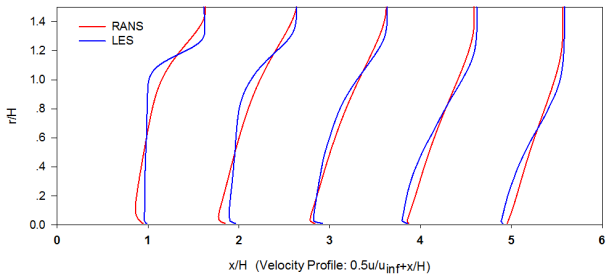

(a) No fan

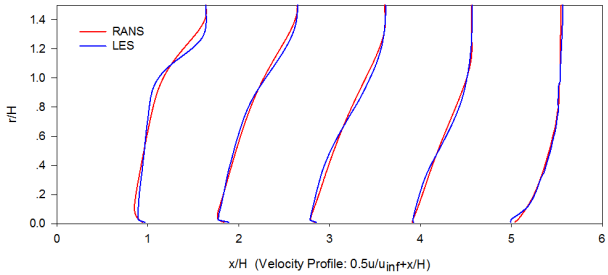

(b) With fan

Fig. 16 Velocity profiles within the recirculation region, from RANS and LES